

# Solute Incorporation at Oxide–Oxide Interfaces Explains How Ternary Mixed-Metal Oxide Nanocrystals Support Element-Specific Anisotropic Growth

Manuel Gliech, Mikaela Görlin, Martin Gocyla, Malte Klingenhof, Arno Bergmann, Sören Selve, Camillo Spöri, Marc Heggen, Rafal E. Dunin-Borkowski, Jin Suntivich, and Peter Strasser\*


**Fundamental understanding of anisotropic growth in oxide nanocrystals is crucial to establish new synthesis strategies and to tailor the nanoscale electronic, magnetic, optical, and electrocatalytic properties of these particles. While several growth investigations of metal alloy nanoparticles have been reported, mechanistic studies on the growth of ternary oxide materials are still missing. This work constitutes the first study on the evolution of anisotropic growth of manganese–cobalt oxide nanoparticles by monitoring the elemental distribution and morphology during the particle evolution via scanning transmission electron microscopy–X-ray spectroscopy. A new growth mechanism based on a “solution-solid-solid” pathway for mixed manganese cobalt oxides is revealed. In this mechanism, the MnO seed formation occurs in the first step, followed by the surface Co enrichment, which catalyzes the growth along the  $\langle 100 \rangle$  directions in all the subsequent growth stages, creating rod, cross-, and T-shaped mixed metal oxides, which preferentially expose  $\{100\}$  facets. It is shown that the interrelation of both Mn and Co ions initializes the anisotropic growth and presents the range of validity of the proposed mechanism as well as the shape-determining effect based on the metal-to-metal ratio.**

## 1. Introduction

Shape-selected oxide nanomaterials have abilities to reveal fundamental growth mechanisms and unique physicochemical properties. Thus, they are of great scientific and technological interest. Because the optical, magnetic, electrical, and catalytic properties of nanomaterials depend sensitively on nanoscale composition, size, and surface terminations,<sup>[1]</sup> the parameter space in which nanomaterials can be designed to unleash new properties beyond bulk is nearly limitless. Nanostructured oxides of the first transition row *d*-elements have received substantial attention to date,<sup>[2]</sup> since they are important functional components in electronics, chemical reactors as well as electrochemical devices. This interest, along with the shift from aqueous to nonhydrolytic and thermal decomposition synthesis routes, have led to significant progress in

Dr. M. Gliech, Dr. M. Görlin, M. Klingenhof, Dr. A. Bergmann,  
Dr. C. Spöri, Prof. P. Strasser  
The Electrochemical Catalysis  
Energy and Materials Science Laboratory  
Department of Chemistry  
Technical University Berlin  
10623 Berlin, Germany  
E-mail: pstrasser@tu-berlin.de  
Dr. M. Gliech, Prof. J. Suntivich  
Department of Materials Science and Engineering  
Cornell University  
Ithaca, NY 14853, USA

Dr. M. Görlin  
Department of Chemistry  
Uppsala University  
Ångström Laboratory  
Uppsala University  
Box 538, 75121 Uppsala, Sweden  
M. Gocyla, Dr. M. Heggen, Prof. R. E. Dunin-Borkowski  
Ernst Ruska Center for Microscopy and Spectroscopy with Electrons  
Forschungszentrum Juelich GmbH  
52425 Juelich, Germany  
Dr. A. Bergmann  
Department of Interface Science  
Fritz Haber Institute of the Max Planck Society  
14195 Berlin, Germany  
S. Selve  
Technische Universität Berlin  
Center for Electron Microscopy (ZELMI)  
Straße des 17. Juni 135, 10623 Berlin, Germany

 The ORCID identification number(s) for the author(s) of this article can be found under <https://doi.org/10.1002/adfm.201909054>.

© 2020 The Authors. Published by WILEY-VCH Verlag GmbH & Co. KGaA, Weinheim. This is an open access article under the terms of the Creative Commons Attribution-NonCommercial-NoDerivs License, which permits use and distribution in any medium, provided the original work is properly cited, the use is non-commercial and no modifications or adaptations are made.

DOI: 10.1002/adfm.201909054

synthesis strategies for controlling the shape and size of binary oxide materials based on fundamental-growth-mechanism understanding.<sup>[3]</sup>

Shape control of metal oxide nanoparticles (NPs) arises from preferred exposure of specific facets. This nanoscale control has been shown to greatly influence surface chemical properties, such as the NPs' ability to catalyze chemical reactions or selectivity towards by promoting specific reaction pathways.<sup>[4]</sup> Deciphering how to control anisotropic nanocrystal (NC) growth, however, has historically been investigated through trial and error because the understanding of NC growth mechanisms at the atomic scale is still elusive. The preparations of distinct oxide morphologies such as rods,<sup>[2b,5]</sup> cubes,<sup>[6,7]</sup> octahedra,<sup>[8]</sup> and others<sup>[9]</sup> have relied on empirical and unsystematically observations. In addition, these studies have often focused on particles with dimensions of several hundred nanometers, since smaller NCs are notoriously harder to control. Clearly, rational design and synthetic strategies for shape-control of oxide nanocrystals based on an atomistic mechanistic understanding are highly desirable.

At present, our understanding of NC growth come from a few systematic studies of experimental synthesis and growth parameters of binary oxides. Notably, the particle size and shape of oxide NCs are affected by inter alia reaction temperature, heating rate, acidity, precursor, solvent, and surfactant selection as well as by their respective individual concentrations,<sup>[10]</sup> while the crystal structure is affected by the precursor selection, temperature, and the gas atmosphere during synthesis.<sup>[11]</sup> However, only a very small number of previous studies have actually addressed and experimentally tracked the atomic-scale growth trajectory of binary oxide crystals and their relevance to oxides with several metals are unclear.<sup>[12]</sup> When considering the goal of elucidating the growth mechanism for rational syntheses, the results from these individual studies do not reveal how different factors affect the NC structure at the atomic level and how it enables anisotropic crystal growth. The lack of molecular insight into growth mechanisms of especially multimetal oxide NCs, in particular with respect to anisotropic growth, has been one of the biggest limiters of our capability to control nanoscale oxide morphologies, and catalytic and other functionalities.

Crystal formation has two distinct evolutionary phases: The nucleation of monomers into seeds and the subsequent particle growth. For growth within liquid phases, the nucleation of seed NCs usually results in thermodynamically controlled Wulff polyhedra to minimize the surface energy. Anisotropy is a result of the kinetics of the subsequent crystal growth phase.<sup>[13]</sup> The two most common mechanistic hypotheses as to anisotropic metal oxide particle growth include: (i) crystallite growth by successive addition of single monomers, wherein the anisotropy arises as a result of different attachment kinetics on surface sites or facets, or (ii) crystallite growth via oriented attachment of preformed smaller crystallites on high energy surfaces.<sup>[14]</sup> Anisotropic growth has also been proposed to occur via a seed mediated solution-liquid solid (SLS) growth process,<sup>[15]</sup> wherein a nucleation seed acts as growth front by which its reaction with monomers form a rod along a single direction. Nonetheless, despite having only a few reports on the mechanism of metal-oxide shape evolution, some even with contradictory results, the growth theory of binary oxides

is generally agreed upon.<sup>[12a,16]</sup> The pace for understanding the shape evolution for ternary oxide NCs and beyond is, however, far behind the state of the binary oxides. Unlike for shaped multimetallic alloy NCs,<sup>[4a,17]</sup> only few studies have focused on the shape-controlled growth of multimetallic oxides NCs, where the interplay of two or more distinct ligand-coordinated metal ions, not metal atoms, controls the shape evolution. This report strives to address this knowledge gap.

In this work, we reveal the complex interplay of ligand-coordinated transition metal ions and how they affect the shape selectivity and morphological evolution of mixed metal oxide NCs and NPs, using MnCoO<sub>x</sub> mixed oxides as model system. Our work presents a detailed atomic-level study of the elemental distribution inside individual NCs during NP growth, using aberration-corrected scanning transmission electron microscopy (STEM) coupled with energy-dispersive X-ray spectroscopy (EDX). In particular, we identify distinctly different phases where Mn and Co ions assemble into a single crystalline NP. We demonstrate the role of elemental heterogeneities on the anisotropic growth in the <100> directions. From our observations we propose a new growth mechanism for ternary oxides, wherein a local Co enrichment acts as the growth front during the directional growth after the nucleation stage which starts from an initially Mn-rich seed. We find that the overall Mn/Co ratio precisely controls the resulting facet and crystal morphology. Furthermore, for the first time in full clarity, we demonstrate the seed formation stage and, in separation, the outgrowth stage, i.e., the crystal branching phenomena. Our insights and conclusions are broadly applicable and can likely provide mechanistic understanding for other shape-controlled oxide growth processes.

## 2. Results and Discussion

### 2.1. Monitoring Morphology and Elemental Distribution during Nanocrystal Growth

Bimetallic MnCoO<sub>x</sub>-NP were prepared by thermal decomposition of Mn(II)-oleate and Co(II)-oleate dispersions in 1-octadecene and oleic acid under protective nitrogen atmosphere.<sup>[3d,11d]</sup> Detailed information on the synthesis procedures can be found in the supplementary information. Aliquots were taken at selected temperatures below the reaction temperature of 300 °C and after 0.1, 1, 2, 5, 10, 20, and 30 min reaction time. The aliquots were immediately quenched with ethanol and the NPs were processed as described in the experimental section.

For samples with a Mn:Co ratio of 1:1, no particle formation was observed below 295 °C. At 295 °C small isolated NPs were observed (Figure S2A, Supporting Information). Bright field transmission electron microscopy (BF-TEM) images show the evolution of the NC growth at 300 °C in **Figure 1A**. After 0.1 min, small cuboctahedrally shaped particles were visible, representing the well-known early nucleation stage (Figure S2B, Supporting Information).<sup>[17,18]</sup> Inductively coupled plasma-optical emission spectroscopy (ICP-OES) revealed a Co-content of 5–7% at the nucleation stage (Figure 1Q) and the X-ray diffraction pattern was consistent with a MnO

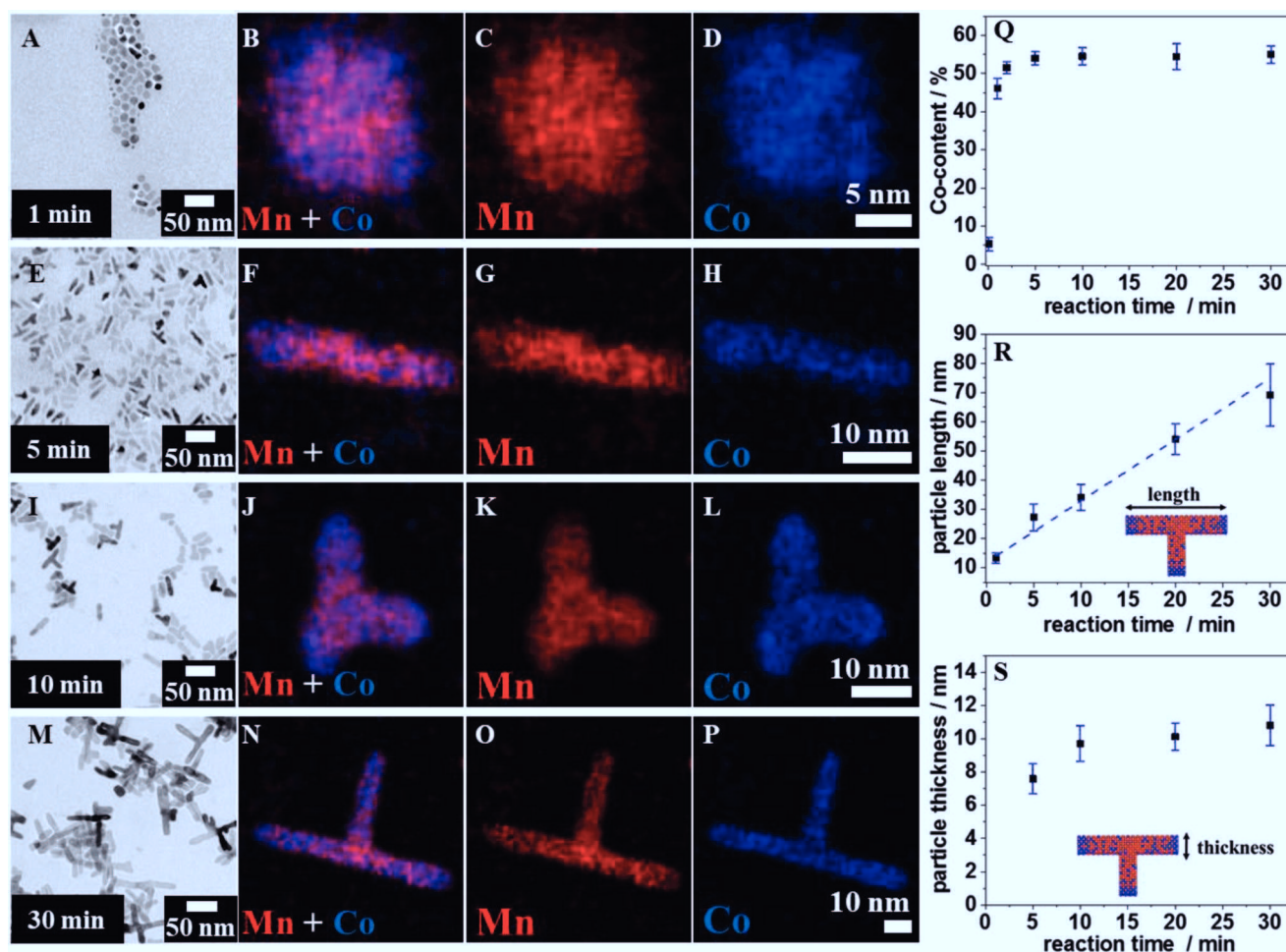


**Figure 1.** A,E,I,M) Bright-field (BF)–TEM images of samples taken after 1, 5, 10, and 30 min reaction time at 300 °C from a reaction aliquot with equal amount of Mn- and Co-oleate precursors. B–D,F–H,J–L,N–P) High-angle annular dark-field (HAADF) HRTEM–EDX elemental mappings showing the intraparticle elemental distribution of Mn (red) and Co (blue). Co enrichments are observed in several areas after 1 min. However, the Co enrichments occur only in the tips of the outgrowths after 5, 10, and 30 min, while the center remains Mn rich. Particle composition and size evolution; Q) evolution of overall cobalt content during particle synthesis (from several syntheses); R) mean particle size and accordingly the particle length along the main axis, the dashed line was inserted to guide the eye. S) Thickness of outgrowth and rods at different reaction times. For particle size, length, and thickness evaluation at least 200 particles have been examined each. HAADF images for the corresponding particles are shown in Figure S1 in the Supporting Information.

structure that contains low amounts of Co (Figure S3, Supporting Information). Already after 1 min, cuboctahedral particles with an average size of 11.5 ( $\pm 1.5$ ) nm and a significant increase in Co-content to 46.1 ( $\pm 2.6$ )% were observed. High angle annular dark field (HAADF)–STEM combined with EDX revealed that these particles exhibit Co enrichments in their outer regions (Figure 1B–D). After 5 min reaction time, the Co content had further increased to 53.3 ( $\pm 1.1$ )%. Here, NPs in rod and branched T shapes with a mean main-axis length of 27.3 ( $\pm 4.6$ ) nm were observed. Interestingly, the Co-enrichments at the tips were consistently observed on both rod and T-shape morphologies and throughout the compositional patterns (Figure 1F–H). Without exceptions, we confirm that the center is Mn-rich, which has acted as the origin of all NPs and the T-shaped outgrowth.

After 10 and 30 min reaction time, both the rod- and T-shaped NCs were observed (Figure 1I–P). At these time points, the Co content has increased slightly to 55% and remained constant

until the end of the synthesis, suggesting a similar incorporation rate of Mn and Co after the branched outgrowths begun forming. It is noteworthy that—despite multiple repeats and careful inspection—no secondary branching was observed in any of the samples, indicating that a single event at the seed stage triggers the anisotropic growth along defined axes. The mean particle length (Figure 1R) shows a linear trend over reaction time, indicating a constant growth rate. This observation suggested that the particle growth was not limited by precursor monomer depletion. The small but continuous increase in the thickness with longer reaction time (Figure 1S) is contraindicative to the growth mechanism based on oriented attachments. The resulting T-branched NPs were all, without exception, single crystalline with Mn-rich centers surrounded by a well-mixed Mn–Co middle section that is capped by Co-rich tips. This compositional and morphological pattern was a robust observation. The branches of the NPs only differed in length depending on growth time.



## 2.2. Orientation and Faceting of Ternary Oxides

To reveal the atomic-scale structure and formation mechanisms of the T branches, detailed high resolution (HR)-TEM analysis of those regions was conducted. **Figure 2A** depicts an image and selected-area-electron diffraction (SAED) pattern of a representative T-shaped NP, demonstrating its single crystalline nature with reflections corresponding to  $\langle 200 \rangle$  and with smaller intensity  $\langle 220 \rangle$  directions. The lattice distances in the tip of the outgrowths appear to be smaller than in the NP center, which can be attributed to the higher Co content in the tips. We next investigate the surfaces of the NPs by aligning the single crystalline NPs to the electron beam as shown in **Figure 2B**. Analysis of several particles revealed that the outgrowths predominantly exposed  $\{100\}$  facets, some of which are connected to adjacent  $\{100\}$  facets by steps of one to three atoms. Additionally, minor fractions of  $\{110\}$  facets are present. The obtained results were confirmed to be reproducible, which validates its accuracy.

## 2.3. Solution-Solid-Solid Mechanism for Anisotropic Oxide Growth

The observed anisotropic mixed-metal-oxide NC morphology and composition patterns cannot be explained by existing conventional growth mechanisms and concepts. If the growth was simply governed by reaction kinetics, assuming similar incorporation rates for Mn and Co, either the outgrowth would be completely intermixed without Co-enrichments, or the crystal branch would have shown a significantly higher Co content along its length to commensurate with the Co-rich tips. On the other hand, if we assume that the incorporation rate for Co-monomer species was higher, an ever-increasing Co-content with longer reaction times should ensue, which is not consistent with our observation. If the anisotropic growth was instead governed by the oriented attachment mechanism, the

initially formed cuboctahedra should be lined up and joined into one single crystal, resulting in alternating Mn and Co-enriched sections, which is also not observed. The appearance of the Co-rich tips and their persistence in the subsequent growth stages is thus inconsistent with oriented attachment. Finally, the small increase in the thickness of the outgrowths (**Figure 1S**) indicates a deposition of monomers rather than crystalline nuclei. In summary, we cannot use existing growth mechanisms to explain our results.

To explain the anisotropies observed, we propose a novel growth mechanism that can account for not just the observations of our shaped mixed metal oxide NCs, but also of past results. **Figure 3** details our proposed mechanism. Initial nucleation generates small MnO seeds with very low Co content, consistent with the X-ray diffraction patterns (see **Figure S3** in the Supporting Information). Subsequently, the Co monomers are preferentially deposited and grow from the  $\{001\}$  facets of the initial seeds, leading to the local Co enrichment and an increase in the overall Co content of the NCs. We did not observe any formation of separately detached CoO NPs via either XRD or TEM. Thus, we conclude the Co-oxide phase must grow from the monomers attached either on the MnO seeds or the  $\text{MnCoO}_x$  NCs. The Co-rich sections on the surface enhance the NC growth rate along the  $\langle 100 \rangle$  direction, producing rods or multi-pods with varying numbers of outgrowths. To explain how the NCs create the outgrowth without affecting the tip composition, we propose that Mn and Co monomers segregate in nearly constant ratios into the buried solid-solid interface between the Co-enriched tip and the linear mixed oxide outgrowth (see **Figure 3**). This mechanism can explain the observed time-invariant Mn:Co ratio of the linear rod outgrowth. In contrast to previously proposed growth mechanisms based on oriented attachment, our model suggests a gradual growth mechanism based on monomer depositions at the Co-enriched sections of the branch tips.

While the proposed growth mechanism may appear similar to the seed-mediated SLS process, our proposed mechanism

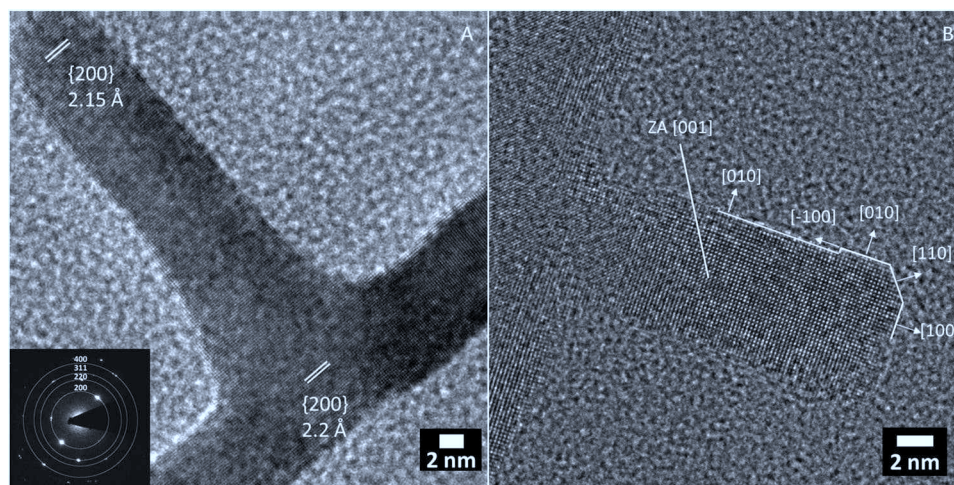


**Figure 2.** A) HRTEM image of  $\text{MnCoO}$ -NP with 56 at% Co. The corresponding SAED pattern showed conformity with expected results for a mixture of PDF#00-048-1719 (CoO) and PDF#01-072-1533 (MnO). The lattice distance in the tip of the outgrowth is smaller than the lattice distance in the region of origin, due to higher Co content in the tips. B) The perfectly aligned columns allow a determination of the exposed facets. The significantly dominant exposed facets are  $\{100\}$ .

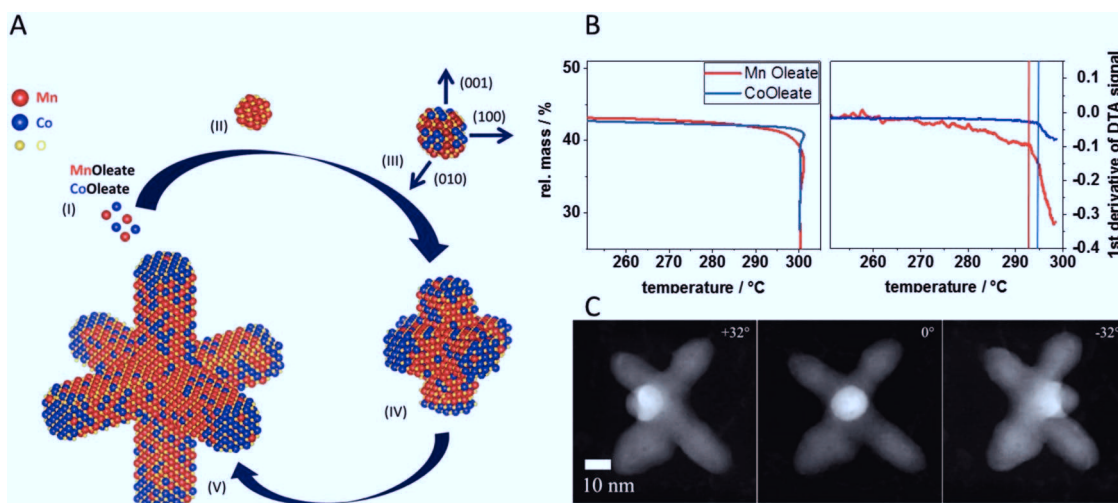


**Figure 3.** A) Structural model of the solution-solid-solid oxide particle nucleation and growth mechanism (SSS): (I) Formation of monomers, Mn (red), Co (blue); (II) Nucleation of small MnO seeds; (III) Delayed deposition and local enrichment of Co on the seed surface; (IV) Formation of outgrowths along the <100> directions with Co enrichments as growth fronts forming multipods; (V) Fully grown MnCoO-NP with Co enrichments as growth fronts well intermixed mid-sections and a Mn rich core; B) Thermogravimetric measurement of Mn-oleate and Co-oleate in a temperature program equivalent to the synthesis conditions; heating rate  $10 \text{ K min}^{-1}$  and  $\text{N}_2$  at  $60 \text{ mL min}^{-1}$ ; corresponding first derivative of the heat flow during thermogravimetric analysis. Abrupt changes in heat flow accompanied by mass loss correspond to decomposition, while small changes without mass change can be assigned to phase changes. C) HAADF images of a multipod under different tilting conditions showing good correspondence with the structural model.

relies on a solid-based growth front as opposed to a liquid metal in the SLS mechanism.<sup>[19]</sup> Most importantly, our model does not rely on the miscibility gap, i.e., the two-phase region that is characteristic of the SLS growth. In fact,  $\text{MnCoO}_x$  forms a solid solution throughout the whole compositional range (see Figure 4), thereby eliminating the possibility of SLS-based  $\text{MnCoO}_x$  growth. In the mechanism we propose, the solid crystalline Co-rich mixed metal oxide serves as the forward-moving growth front instead. We will now refer to this mechanism as the solution-solid-solid oxide mechanism (SSS). Beyond our present data, our mechanism also explains previous empirical reports on shaped oxide morphologies, where no mechanistic picture so far has been provided.<sup>[6b,16,20]</sup>

Our hypothesis is further supported by thermal gravimetric analysis (TGA) combined with differential scanning

calorimetry (DSC) investigations using conditions that simulate the synthetic protocol of the shaped NCs. The relative mass loss and the first derivative of the heat flow are shown in Figure 3B. The change in heat flow above  $270^\circ\text{C}$  prior to mass loss in the Mn-oleate sample suggests a phase-transition point that corresponds to the monomer formation. At  $293^\circ\text{C}$ , the heat flow changes abruptly indicating precursor decomposition, which is consistent with the observed mass loss in the TGA. In contrast, the Co-oleate precursor remains unchanged until  $297^\circ\text{C}$ . At this point, we observed the decomposition-induced mass loss concomitant with the heat-flow signal of the Co precursor. Our TGA–DSC investigations hence agree well with the TEM experiment, showing that Mn is responsible for initializing the nucleation process, followed by Co deposition.

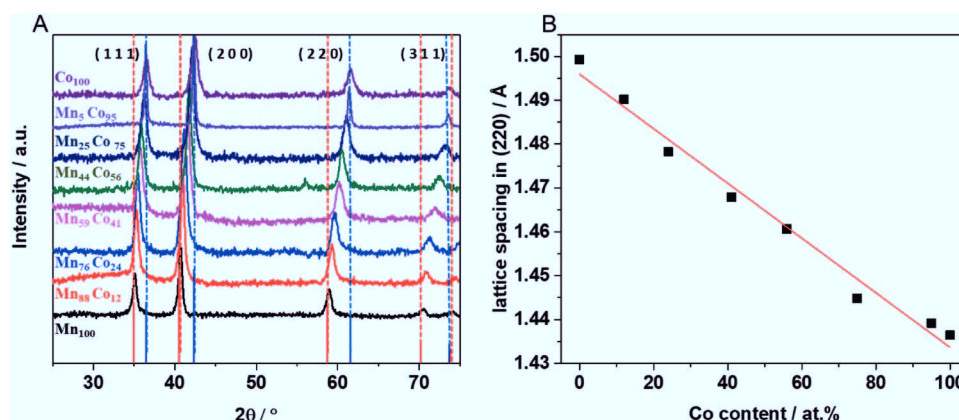


**Figure 4.** X-ray diffraction patterns of MnCoO-NP A) and lattice spacing along [220] B) in samples with different metal to metal ratios determined with ICP-OES. The patterns of the single metal oxides show conformity with PDF#00-048-1719 (CoO) and PDF#01-072-1533 (MnO). The linear shift in lattice spacing shows complete miscibility in accordance with Vegard's law. Broadening of the reflections in the Mn–Co oxides are due to the observed Mn- and Co-enriched sections of the NPs. The additional reflection at a  $2\theta$  value of  $57^\circ$  in the sample with 56 at% Co is accounted for by the Si substrate.

To further validate our proposed growth mechanism of shaped mixed-metal-oxide NCs, a Co-oleate molar equivalent of 0.2 was injected into a progressing NC synthesis mixture containing solely Mn-Oleate after 2 min of reaction time. According to our mechanistic hypothesis, the synthesis mixture should be dominated by cuboctahedrally shaped MnO-NPs prior to the Co-oleate injection. When the Co-oleate is injected, we expect to observe the emergence of the Co-rich branches and the outgrowths from the MnO seeds. Indeed, consistent with our predictions, an aliquot taken right before the Co-oleate injection contained both cuboctahedral as well as edged single crystalline MnO-NPs, see Figure S4A in the Supporting Information. After the Co-oleate precursor is injected, the sample at the end of the synthesis display the expected outgrowths along the  $\langle 100 \rangle$  directions (see Figure S4B,C and Figure S5 in the Supporting Information). The EDX elemental maps of Mn (red) and Co (blue) (Figure S4D–F, Supporting Information) demonstrated the deposition of Co along the corners and edges of the seed particles with only little Co population on the lateral faces. As expected from our hypothesis, the outgrown branches contained Co-rich tips and the intermixed Co–Mn oxide sections between the tips and the core where the branching commenced. These results are in line with our proposed growth mechanism.

We further investigated the anisotropic shape evolution as a function of Mn:Co ratio. For comparison we also prepared the binary oxide NCs (Figures S6 and S7, Supporting Information). Binary  $\text{MnO}_x$  NPs had cuboctahedral shapes and exhibited a narrow size distribution. In comparison, binary  $\text{CoO}_x$  NPs had octahedral shapes, but with considerably more defined edges, and arranged as “flower-like” agglomerates in agreement with previous work.<sup>[21]</sup> In both materials, increasing oleic acid concentration causes the edges to be less distinct. Unlike previous reports<sup>[12a,16]</sup> we did not observe any formation of multipod in the binary Mn or Co oxides samples either with or without additional oleic acid, over a very broad range of surfactant (oleic acid) to precursor ratios. We thus speculate that minor metal-ion impurities and/or functional groups in the precursor solutions may have played a role on the decomposition of the precursor during the synthesis, which corroborate well the previously reported morphology-controlling effects of additives by Schaak and co-workers.<sup>[11d]</sup>

To provide further support for the proposed anisotropic growth of Mn–Co oxides, X-ray diffraction patterns of oxide NCs with different Mn to Co ratios were conducted (Figure 4) to reveal insights into their crystal structure. All NPs showed exclusively Bragg reflections assigned to a face-centered cubic (fcc) NaCl structure (space group:  $\text{Fm}\bar{3}\text{m}$ ) with peaks shifting to higher  $2\theta$  values with increasing Co content in the NCs. Importantly, while the lattice constants changed linearly with the Co content, the shape of the Bragg reflections of the investigated mixed metal oxides appeared asymmetric. The former indicates complete, statistical miscibility of Co and Mn ions in the oxide lattice over the entire range of Mn to Co ratios in compliance with Vegard’s law, while the latter can be attributed to the small Mn- and Co-rich sections within the NPs. The presented XRD patterns in Figure 4 show the ability of the oxide structure to accommodate full ternary-oxide composition range, in agreement with our proposed mechanism

(no thermodynamic phase separation). Crystallite domain sizes were determined using the Scherrer Equation and range from 9.6 to 23.1 nm, which are in good agreement with the thickness of the outgrowths from TEM images (Table S1, Supporting Information).

NPs prepared from mixtures of Mn- and Co-oleates, keeping all other reaction conditions constant, showed the preferred crystal growth trajectory along the  $\langle 100 \rangle$  directions in a compositional range between 12 and 56 at% of Co (see Figure 5). This preference results in a gradual change from hexapod-, to cross-, to T-shaped, and finally to linear rod-shaped nanocrystals as the dominant morphology. With the Co content approaching 56 at%, the number of outgrowth from the center decreased steadily. The elemental distributions of the samples with 12, 41, and 56 at% Co showed Co-enriched tips and Mn-rich centers, in line with our proposed new growth mechanism.

We now provide a postulate on an interesting observation that the branching and outgrowth decrease at higher Co concentration in the mixed Mn–Co NCs. With increasing Co concentration, between 12 and 56 at% Co, the formation of the Co-rich domains on the surface of the Mn-rich seeds becomes more favorable. Consequently, it accelerates the formation of the Co-rich domains that catalyze the formation of mixed-metal-oxide outgrowths. This rapid outgrowth formation occurs before other adjacent NC regions have enough time to accumulate sufficient Co to support outgrowths in other directions. The result of this “the-winner-takes-all” scenario is that the formation of the first outgrowth(s) suppresses additional branching in other directions. This stands in contrast to the situation at low Co concentration, where the slow formation of the Co-rich region allows several areas to be simultaneously enriched before one outgrowth emerges. Thus, when the first outgrowth develops, several regions have already accumulated sufficient Co and can readily support additional outgrowths in other directions, leading to a higher number of outgrowths with similar length, such as hexapods.

At higher Co concentration (e.g., >75 at%), the morphology of the NCs is close to that of pure CoO NPs with flower-like agglomeration of individual particles. Only few particles have discernible outgrowths and no enriched sections are visible. This finding suggests that the particle formation and growth at >75 at% Co is mostly ruled by the growth of CoO wherein Mn ions are incorporated into the CoO. That observation is in contrast to the SSS mechanism, which dominates the growth at lower Co concentrations.

In the SSS mechanism, Mn and Co ions migrate to the Co-enriched area at the branch tips, where they are integrated into the lattice at the heterogeneous interface between the outgrowth branch and the Co-enriched tip. This process continuously occurs to prolong the branch. We emphasize that a direct monomer incorporation into the Co-enriched tip or the simultaneous attachment of Co at the tip to maintain the enriched growth front cannot account for our findings in NPs with low Co content; as shown in Figure 5M, the Co is distinctive in the branch tips and only very little present in the rest of the particle. Figure 6 shows a schematic of our proposed mechanism, which highlights the interdependency of the Mn and Co on the NC evolution to account for the emerging morphologies and elemental distributions.



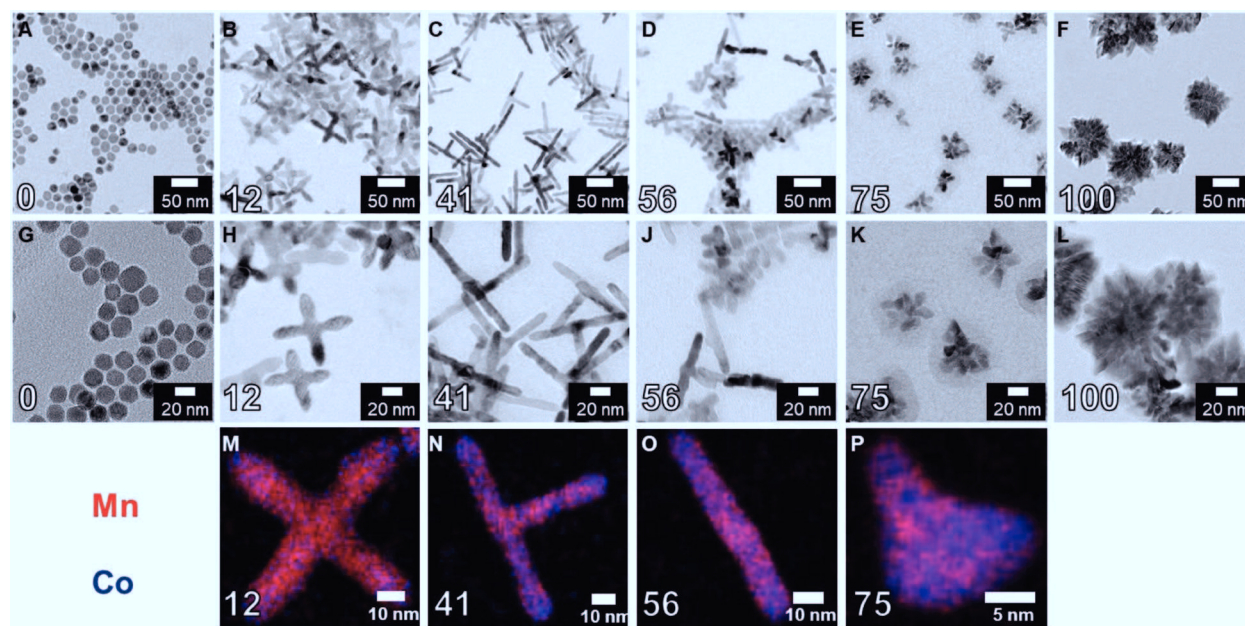


**Figure 5.** BF-TEM images of MnCoO NPs with 0, 12, 41, 56, 75, and 100 at%Co (left to right, at% Co indicated in white numbers) after 30 min reaction time. A–F) Typical low-magnification TEM images and G–L) corresponding higher resolution images. MnO NPs have a cuboctahedral shape with a narrow size distribution; CoO NPs are octahedrally shaped, with considerably defined edges arranged in “flower-like” agglomerates. Mixtures of Mn- and Co-oleate induce a preferred growth along the  $\langle 100 \rangle$  direction of the crystal and therefore have multipod-, cross-, T-, and rod-shaped NPs as dominant motif, depending on the Mn/Co ratio. M–P) HAADF HRTEM-EDX mappings of mixed oxide NPs (Mn in red, Co in blue). The ends of the outgrowths show Co-enrichments while the center of the NP has a lower than average Co content in samples with 12, 41, and 56 at% Co. The sample with 75 at% Co shows no enriched sections. HAADF images for the corresponding particles are shown in Figure S8 in the Supporting Information.

### 3. Conclusion

In conclusion, we report the nucleation-and-growth mechanism of highly anisotropic bimetallic Mn–Co oxide NPs, a

materials family important for several energy and catalysis applications. The NC branching is ascribed to the formation of a Co-enriched tip of the branching, which serve as the growth front of the NCs. This Co-rich tip originates from the

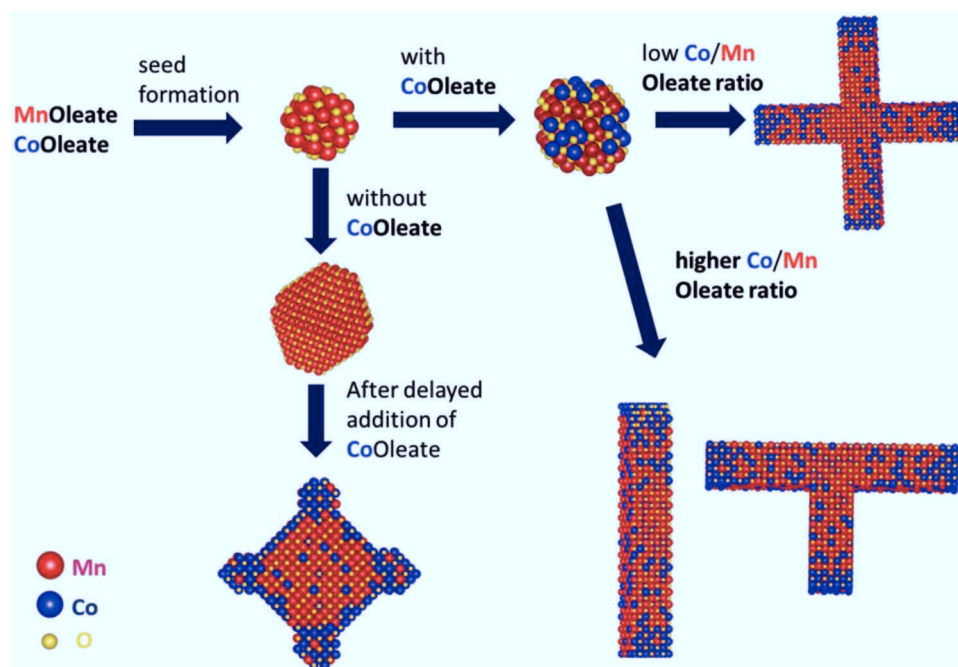


**Figure 6.** Schematic representation of morphological dependencies on metal to metal precursor ratio, the point of intermixture and the intraparticle elementary distribution.

Mn-rich seeds despite the two oxides being miscible. Existing continuous growth or oriented-attachment mechanism cannot explain the observed anisotropic composition and morphology. Thus, we suggest a new mechanism—the solution-SSS oxide growth mechanism—whereby the initial MnO seed formation supports Co-enriched surfaces, which act as growth catalyst along the <100> directions. This preferential growth anisotropy persists through all subsequent growth stages, resulting in anisotropically shaped ternary oxides. We demonstrate that the metal-to-metal ratio can influence the morphology of the NPs, highlighting the importance of the second metal on the anisotropic growth along a certain trajectory of oxide nanomaterials over the surfactants, which were observed to play a less important role on the anisotropy in our experiment. The proposed SSS growth mechanism is likely paradigmatic for other mixed oxide systems and could enable new guidelines for rational syntheses of anisotropic morphologies and compositional patterns. We envision new possibilities in how this advancement can improve future NP design—a multitude of advances for oxide applications such as enhanced battery materials, supercapacitors,<sup>[22]</sup> and multifunctional catalysts.

## 4. Experimental Section

**Synthesis of Manganese and Cobalt Oleate Precursors:** The metal oleate precursors were prepared by dissolving sodium oleate ( $20 \times 10^{-3}$  M) and either manganese(II)chloride (Sigma Aldrich,  $\geq 99\%$ , trace metal basis) or cobalt(II)chloride-hexahydrate (Roth,  $\geq 99\%$ ) (10 mmol) respectively in a mixture of ethanol (40 mL), water (30 mL), and n-hexane (30 mL). The solution was heated to 65 °C and held at that temperature for 3 h under reflux. The cooled solution was transferred and washed gently with water, sonicated and centrifuged several times, until no solid phase was observed between the organic and aqueous phase. A sample of the viscous product was taken to determine the metal concentration. Afterwards the product was stored in a fridge.

**Synthesis of Metal Oxide NPs:** The required amount of each precursor with respect to the resulting metal concentration was transferred into a three-neck flask and heated to 115 °C for 1 h. The dry residue was redissolved in 1-octadecene and oleic acid. The mixture was heated to 160 °C with  $10 \text{ K min}^{-1}$  under constant nitrogen flow. The temperature was held for 20 min. The temperature was subsequently increased at a rate of  $10 \text{ K min}^{-1}$  to 300 °C under reflux and constant nitrogen flow. In order to investigate the growth pathway of the cross-, T-, and rod-shaped manganese–cobalt mixed oxide NCs, aliquots were taken at different reaction times during the synthesis and immediately quenched in ethanol. The NCs were collected by centrifugation at 7800 rpm and then washed several times with cyclohexane and ethanol. After 30 min the remaining mixture was quenched in ethanol and processed as described for the aliquots. The respective precipitates were ultimately dispersed in cyclo-hexane.

**Synthesis of Mixed Metal Oxide NPs with Delayed Co Oleate Addition:** Manganese oleate precursor was transferred into a three-neck flask and heated to 115 °C for 1 h. The dry residue was redissolved in 1-octadecene and oleic acid. The mixture was heated to 160 °C with  $10 \text{ K min}^{-1}$  under constant nitrogen flow. The temperature was held for 20 min. The temperature was subsequently increased at a rate of  $10 \text{ K min}^{-1}$  to 300 °C under reflux and constant nitrogen flow. After 2 min an aliquot was taken and immediately quenched in ethanol. Cobalt oleate precursor was heated to 115 °C for 1 h. The dry residue was redissolved in 1-octadecene and oleic acid. Cobalt oleate was injected into the MnO-NP synthesis after 2 min reaction time. After 30 min reaction time the NCs were collected by centrifugation at 7800 rpm and then washed several times with cyclohexane and ethanol. After

30 min the remaining mixture was quenched in ethanol and processed as described for the aliquots. The respective precipitates were ultimately dispersed in cyclo-hexane.

**Thermogravimetric Analysis and Differential Scanning Calorimetry:** TGA–DSC were conducted in a PerkinElmer STA-8000. The measurements were performed in nitrogen with heating rates according to the synthesis protocol. Accuracy and reproducibility were improved using a four step procedure: (1) Heating the empty crucible to 1100 °C, holding for 1 h, and subsequent cooling to room temperature. (2) The thermal program emulating the synthesis was run with that empty crucible. (3) Repetition of step 1. (4) Insertion of the sample and running the thermal program.

**Composition Confirmation:** ICP-OES: Compositional analysis was performed using a 715-ES ICP analysis system (Varian). The standard concentrations were 1, 0.1, and 0.01 ppm for manganese and cobalt. The chosen wavelengths for concentration determination were 257.61; 259.37, 294.92 nm for manganese and 228.62; 236.38; 237.86; 238.89 nm for cobalt. The samples of unsupported NPs were prepared by drying 100  $\mu\text{L}$  of the NP dispersion, addition of 400  $\mu\text{L}$  freshly prepared aqua regia and dilution to 10 mL with water.

**Microscopy and Spectroscopy:** Conventional TEM was performed on a FEI Tecnai G<sup>2</sup> 20 S-TWIN with LaB<sub>6</sub> cathode, 200 kV accelerating voltage. For preparation, a holey carbon Cu grid with 200 mesh was used. The electron microscope includes an EDX with an EDAX r-TEM SUTW Detector. STEM was performed using a FEI Titan 80–200 (“ChemSTEM”<sup>[23]</sup>) electron microscope with a Cs-probe corrector (CEOS GmbH) and an HAADF detector. The microscope was operated at 200 kV. In order to achieve “Z-Contrast” conditions, a probe semiangle of 25 mrad and an inner collection semi angle of the detector of 88 mrad were used. Compositional maps were obtained with EDX using four large-solid-angle symmetrical Si drift detectors. For EDX elemental mapping, Co K and Mn K peaks were used. Structural models of the manganese cobalt oxide nanoparticles at different growth stages were generated using the VESTA (Visualization for Electronics and Structural Analysis) software.<sup>[24]</sup>

## Supporting Information

Supporting Information is available from the Wiley Online Library or from the author.

## Acknowledgements

This work was supported by the Federal Ministry of Education and Research under the grant reference number 03SF0433A “MEOKATS”. M.H. and M.G. thank the Deutsche Forschungsgemeinschaft (DFG) for financial support within the grant HE7192/1-1. The authors thank the Zentraleinrichtung für Elektronenmikroskopie (Zelmi) of the Technical University Berlin for their support with TEM and EDX measurements.

## Conflict of Interest

The authors declare no conflict of interest.

## Author Contributions

M.G., P.S., and J.S. conceived and coordinated the study. M.G., M.G., M.K., A.B., and C.S. conducted experiments, carried out the experimental work and data analysis. M.G., M.H., and R.E.D.-B. carried out HAADF-TEM and EDX-mappings. S.S. supervised and conducted high-resolution transmission electron microscopy. All authors discussed the results and commented on the manuscript. M.G., J.S., and P.S. wrote the manuscript with the contribution of all co-authors.



## Keywords

anisotropic oxide, elemental mapping, faceted single-crystal, growth mechanism

Received: October 31, 2019

Revised: December 4, 2019

Published online: January 20, 2020

- [1] a) L.-s. Li, J. Hu, W. Yang, A. P. Alivisatos, *Nano Lett.* **2001**, 1, 349; b) A. P. Alivisatos, *Science* **1996**, 271, 933.
- [2] a) Y. K. Mishra, S. Kaps, A. Schuchardt, I. Paulowicz, X. Jin, D. Gedamu, S. Wille, O. Lupan, R. Adelung, *KONA Powder Part. J.* **2014**, 31, 92; b) Y. Li, W. Shen, *Chem. Soc. Rev.* **2014**, 43, 1543; c) H. Yang, Z.-H. Liu, *Cryst. Growth Des.* **2010**, 10, 2064.
- [3] a) R. Deshmukh, M. Niederberger, *Chem. - Eur. J.* **2017**, 23, 8542; b) M. Niederberger, N. Pinna, *Metal Oxide Nanoparticles in Organic Solvents: Synthesis, Formation, Assembly and Application*, Springer, London **2009**; c) M. Niederberger, G. Garnweitner, *Chem. - Eur. J.* **2006**, 12, 7282; d) J. Park, K. An, Y. Hwang, J.-G. Park, H.-J. Noh, J.-Y. Kim, J.-H. Park, N.-M. Hwang, T. Hyeon, *Nat. Mater.* **2004**, 3, 891; e) S. G. Kwon, T. Hyeon, *Acc. Chem. Res.* **2008**, 41, 1696.
- [4] a) C. Cui, M. Ahmadi, F. Behafarid, L. Gan, M. Neumann, M. Heggen, B. R. Cuenya, P. Strasser, *Faraday Discuss.* **2013**, 162, 91; b) A. S. Varela, W. Ju, T. Reier, P. Strasser, *ACS Catal.* **2016**, 6, 2136; c) F. S. Roberts, K. P. Kuhl, A. Nilsson, *ChemCatChem* **2016**, 8, 1119; d) K. A. Stoerzinger, O. Diaz-Morales, M. Kolb, R. R. Rao, R. Frydendal, L. Qiao, X. R. Wang, N. B. Halck, J. Rossmeisl, H. A. Hansen, T. Vegge, I. E. L. Stephens, M. T. M. Koper, Y. Shao-Horn, *ACS Energy Lett.* **2017**, 2, 876.
- [5] a) F. Dumestre, B. Chaudret, C. Amiens, M.-C. Fromen, M.-J. Casanove, P. Renaud, P. Zurcher, *Angew. Chem., Int. Ed.* **2002**, 41, 4286; b) M. S. El-Deab, M. I. Awad, A. M. Mohammad, T. Ohsaka, *Electrochem. Commun.* **2007**, 9, 2082.
- [6] a) L. Xiaohe, Q. Guanzhou, L. Xingguo, *Nanotechnology* **2005**, 16, 3035; b) N. Bao, L. Shen, W. An, P. Padhan, C. Heath Turner, A. Gupta, *Chem. Mater.* **2009**, 21, 3458.
- [7] J. A. Bau, P. Li, A. J. Marengo, S. Trudel, B. C. Olsen, E. J. Luber, J. M. Buriak, *Chem. Mater.* **2014**, 26, 4796.
- [8] a) H. Liu, X. Zhu, M. Li, Q. Tang, G. Sun, W. Yang, *Electrochim. Acta* **2014**, 144, 31; b) F. Gao, R. Liu, J. Yin, Q. Lu, *Sci. China: Chem.* **2014**, 57, 114.
- [9] Z. Chen, Z. Jiao, D. Pan, Z. Li, M. Wu, C.-H. Shek, C. M. L. Wu, J. K. L. Lai, *Chem. Rev.* **2012**, 112, 3833.
- [10] a) M. Liu, H. C. Zeng, *Cryst. Growth Des.* **2012**, 12, 5561; b) H. Zhang, L. Jing, J. Zeng, Y. Hou, Z. Li, M. Gao, *Nanoscale* **2014**, 6, 5918.
- [11] a) Y.-w. Jun, Y.-y. Jung, J. Cheon, *J. Am. Chem. Soc.* **2002**, 124, 615; b) M. Gliech, A. Bergmann, C. Spöri, P. Strasser, *J. Energy Chem.* **2016**, 25, 278; c) Y.-w. Jun, J.-s. Choi, J. Cheon, *Angew. Chem., Int. Ed.* **2006**, 45, 3414; d) M. R. Buck, A. J. Bicch, R. E. Schaak, *Chem. Mater.* **2014**, 26, 1492.
- [12] a) T. Ould-Ely, D. Prieto-Centurion, A. Kumar, W. Guo, W. V. Knowles, S. Asokan, M. S. Wong, I. Rusakova, A. Lüttge, K. H. Whitmire, *Chem. Mater.* **2006**, 18, 1821; b) T. D. Schladt, T. Graf, W. Tremel, *Chem. Mater.* **2009**, 21, 3183.
- [13] G. Wulff, *Z. Kristallogr. Mineral.* **1901**, 34, 449.
- [14] R. L. Penn, J. F. Banfield, *Geochim. Cosmochim. Acta* **1999**, 63, 1549.
- [15] a) T. J. Trentler, K. M. Hickman, S. C. Goel, A. M. Viano, P. C. Gibbons, W. E. Buhro, *Science* **1995**, 270, 1791; b) T. J. Trentler, S. C. Goel, K. M. Hickman, A. M. Viano, M. Y. Chiang, A. M. Beatty, P. C. Gibbons, W. E. Buhro, *J. Am. Chem. Soc.* **1997**, 119, 2172; c) J. D. Holmes, K. P. Johnston, R. C. Doty, B. A. Korgel, *Science* **2000**, 287, 1471.
- [16] D. Zitoun, N. Pinna, N. Frolet, C. Belin, *J. Am. Chem. Soc.* **2005**, 127, 15034.
- [17] L. Gan, C. H. Cui, M. Heggen, F. Dionigi, S. Rudi, P. Strasser, *Science* **2014**, 346, 1502.
- [18] E. Ringe, R. P. Van Duyne, L. D. Marks, *Nano Lett.* **2011**, 11, 3399.
- [19] Z. Li, Y. Ding, Y. Xiong, Y. Xie, *Cryst. Growth Des.* **2005**, 5, 1953.
- [20] C.-H. Kuo, I. M. Mosa, S. Thanneeru, V. Sharma, L. Zhang, S. Biswas, M. Aindow, S. Pamir Alpay, J. F. Rusling, S. L. Suib, J. He, *Chem. Commun.* **2015**, 51, 5951.
- [21] Y. Zhang, J. Zhu, X. Song, X. Zhong, *J. Phys. Chem. C* **2008**, 112, 5322.
- [22] S. D. Perera, X. Ding, A. Bhargava, R. Hovden, A. Nelson, L. F. Kourkoutis, R. D. Robinson, *Chem. Mater.* **2015**, 27, 7861.
- [23] E. R.-C. f. M. a. s. w. Electrons, *J. Large-Scale Res. Facil.* **2016**, 2, A43.
- [24] K. Momma, F. Izumi, *J. Appl. Crystallogr.* **2011**, 44, 1272.